Nanoscale

PAPER

View Article Online
View Journal | View Issue

Cite this: *Nanoscale*, 2020, **12**, 22258

Influence of 4f filling on electronic and magnetic properties of rare earth-Au surface compounds†

L. Fernandez, [a,d] M. Blanco-Rey, [b,c] R. Castrillo-Bodero,[c,d] M. Ilyn,[c,d] K. Ali, [c,d] E. Turco, [d] M. Corso, [c,d] M. Ormaza, [a] P. Gargiani,[e] M. A. Valbuena, [f,g] A. Mugarza, [f,h] P. Moras, [i] P. M. Sheverdyaeva, [i] Asish K. Kundu, [i] M. Jugovac, [i] C. Laubschat,[j] J. E. Ortega [a,d] and F. Schiller *[c,d]

Received 1st July 2020,
Accepted 12th October 2020

DOI: 10.1039/d0nr04964f

rsc.li/nanoscale

One-atom-thick rare-earth/noble metal (RE-NM) compounds are attractive materials to investigate two-dimensional magnetism, since they are easy to synthesize into a common RE-NM_2 structure with high crystal perfection. Here we perform a comparative study of the $GdAu_2$, $HoAu_2$, and $YbAu_2$ monolayer compounds grown on Au(111). We find the same atomic lattice quality and moiré superlattice periodicity in the three cases, but different electronic properties and magnetism. The $YbAu_2$ monolayer reveals the characteristic electronic signatures of a mixed-valence configuration in the Yb atom. In contrast, $GdAu_2$ and $HoAu_2$ show the trivalent character of the rare-earth and ferromagnetic transitions below 22 K. Yet, the $GdAu_2$ monolayer has an in-plane magnetic easy-axis, *versus* the out-of-plane one in $HoAu_2$. The electronic bands of the two trivalent compounds are very similar, while the divalent $YbAu_2$ monolayer exhibits different band features. In the latter, a strong 4f–5d hybridization is manifested in neatly resolved avoided crossings near the Fermi level. First principles theory points to a residual presence of empty 4f states, explaining the fluctuating valence of Yb in the $YbAu_2$ monolayer.

1. Introduction

Rare-earth/noble-metal (RE-NM) monolayer-thick alloys can be readily synthesized by low-temperature vapor epitaxy on the (111) surface of Cu, Ag, and Au single crystals, leading to a rich family of surface compounds.[1–6] They all share a common, well-defined structure and excellent crystal quality with a RE-NM_2 stoichiometry, as a well as a hexagonal moiré with a nanoscale periodicity that is induced by the lattice mismatch between the RE-NM_2 monolayer and the noble metal substrate. This structural homogeneity among the series of lanthanides makes the RE-NM_2 monolayer a convenient platform to tune spin textures and magnetic properties of great interest in the field of spintronics,[7] while their chemical stability and moiré modulation convert these compounds into suitable magnetic templates to drive self-organized nanostructure growth.[8–11] At a more fundamental level, the crystal perfection and identical structure of the RE-NM_2 monolayer among the REs appear ideal to investigate the interplay between electronic properties and magnetism, that is, the connection between 4f shell filling, f–d hybridization, RE atom valency and magnetic response in two dimensions. This is of major interest in materials exhibiting competing magnetic and electronic phases around quantum critical points, such as heavy-fermion metals.[12] In particular, the Ho case is of recent interest due to its high angular magnetic moment and its unconventional magnetic properties.[13–16]

In the present work we carry out a comparative analysis of $GdAu_2$, $HoAu_2$ and $YbAu_2$ monolayers epitaxially grown on a Au(111) surface. By means of angle resolved photoemission spectroscopy (ARPES) and density functional theory (DFT) we investigate the characteristic signatures of the band structure

[a]*Universidad del País Vasco UPV-EHU, Dpto. Física Aplicada I, 20018 San Sebastián, Spain*
[b]*Universidad del País Vasco UPV-EHU, Dpto. de Polímeros y Materiales Avanzados: Física, Química y Tecnología, 20018 San Sebastián, Spain*
[c]*Donostia International Physics Center, 20018 Donostia-San Sebastián, Spain. E-mail: frederikmichael.schiller@ehu.es*
[d]*Centro de Física de Materiales CSIC/UPV-EHU-Materials Physics Center, 20018 San Sebastián, Spain*
[e]*ALBA Synchrotron Light Source, Carretera BP 1413 km 3.3, 08290 Cerdanyola del Vallès, Spain*
[f]*Catalan Institute of Nanoscience and Nanotechnology (ICN2), CSIC and The Barcelona Institute of Science and Technology, Campus UAB, Bellaterra, 08193 Barcelona, Spain*
[g]*IMDEA Nanociencia, 28049 Madrid, Spain*
[h]*Institució Catalana de Recerca i Estudis Avançats (ICREA), 08070 Barcelona, Spain*
[i]*Istituto di Struttura della Materia, Consiglio Nazionale delle Ricerche, 34149 Trieste, Italy*
[j]*Institut für Festkörper- und Materialphysik, Technische Universität Dresden, 01062 Dresden, Germany*

†Electronic supplementary information (ESI) available. See DOI: 10.1039/D0NR04964F

that define the valence state of the RE atom in the compound, whereas element-sensitive X-ray magnetic circular dichroism (XMCD) is used to probe the magnetic order and determine magnetic anisotropy. For Gd and Ho we find a trivalent electronic configuration in $GdAu_2$ and $HoAu_2$, respectively, and a clear ferromagnetic behavior. However, the magnetization axis is out-of-plane for Ho and in-plane for Gd, reflecting their respective 4f shell filling and orbital moment. $YbAu_2$ behaves notably different. Yb is known to exhibit a variable valence state, ranging from Yb^{2+}, *e.g.*, in bulk Yb metal[17] to Yb^{3+} in oxides,[18] *via* a fluctuating (or mixed) valence configuration in metal alloys.[19–22] In the $YbAu_2$/Au(111) monolayer system we find a mixed valence for Yb, close to divalency, which we attribute to f–d hybridization around the Fermi level E_F.

2. Experimental and computational details

The different RE-Au_2 surface compounds were grown *in situ* under ultra-high vacuum ($p < 2 \times 10^{-10}$ mbar) conditions by evaporation of small amounts of RE atoms on the Au(111) surface which was hold at a fixed temperature. The optimal growth temperature of the substrate varies between 400 and 450 °C for $GdAu_2$, around 420 °C for $HoAu_2$ and at 300 °C for $YbAu_2$. Below these temperatures, the characteristic moiré was not well formed, and above them the RE metals diffuse into the bulk or re-evaporate under vacuum. Several Au(111) samples were used in order to avoid contamination from other RE atoms used in previous experiments.‡

Preparation and analysis of the samples were performed in different experimental systems and laboratories. Photoemission data were acquired at two home laboratories (CFM San Sebastian, Universität Zürich) using Helium Iα and IIα excitation lines ($h\nu$ = 21.2 eV and 40.8 eV, respectively), and at the VUV-Photoemission beamline of the Elettra Synchrotron in Trieste, Italy. In San Sebastian and Trieste a channel plate-based display type hemispherical analyzer was used with angular and energy resolution set to 0.1° and 40 meV, respectively, while in Zürich a hemispherical analyzer with six channeltrons was employed.[23] At the synchrotron, *p*-polarized light was used and the sample temperature during measurements was 17 K. Scanning tunneling microscopy (STM) experiments were carried out at 300 K in San Sebastian using an Omicron VT Setup. XMCD experiments were realized at the BOREAS beamline of ALBA synchrotron, Spain. There, the samples were prepared *in situ* and their quality was checked with low energy electron diffraction (LEED) prior to the XMCD measurements. Absorption spectra were acquired in total electron yield at two beam-incidence geometries, namely out-of-plane for normal incidence and in-plane for 70° incidence. The applied magnetic field direction was collinear to the light propagation. In all cases 90% circularly polarized light from a helical undulator was used. The measurements were carried out between 2 and 25 K with a variable magnetic field up to ±6 T.

Band structures of free-standing $YbAu_2$ monolayers and $YbAu_2$/Au(111) stacks were obtained from first-principles DFT calculations with the PBE exchange and correlation functional.[24] The FLEUR code,[25] based on the full-potential linearized augmented plane wave (FLAPW) formalism,[26,27] was used. Spin–orbit interactions were included self-consistently in the calculations with spins aligned perpendicular to the surface.[28] The FLAPW basis set was constructed with a bidimensional 9 × 9 × 1 Monkhorst–Pack *k*-point mesh[29] and plane wave expansion cutoffs of 109 eV for the wavefunctions, and 272 eV for the density and potential. For the local basis, Yb-6s,4f,5d and Au-6s,5d electrons were included as valence electrons, and Yb-5s,5p and Au-5p as linear orbitals. Muffin tin sphere radii of 1.35 Å were used for Yb and Au, and l_{max} = 10 in the partial wave expansions. The Fermi energy was determined by the triangular method. Additional calculations were carried out in the GGA+U approximation[30–32] (see the ESI†). As in previous works with Gd-based compounds,[3] we used the experimentally-determined lattice constant of the compound (5.4 Å) to fix the same in-plane atomic distance for the $REAu_2$ monolayer and the $REAu_2$/Au(111) slab. For $YbAu_2$ on one or several Au substrate layers (supported $YbAu_2$), results presented here correspond to vertical fcc stacking, using 2.25 Å interlayer distance. Yet, we also checked $YbAu_2$/Au(111) with Yb atoms in top stacking, as well as small variations of the geometry parameters, but no significant changes were obtained.

3. Results and discussion

3.1. Structure

Representative low-energy electron diffraction patterns and scanning tunneling microscopy images for structurally-optimal $HoAu_2$ and $YbAu_2$ monolayers are shown in Fig. 1. The LEED images reveal the characteristic $(\sqrt{3} \times \sqrt{3})R30°$ reconstruction of the 2D RE-Au_2 compounds (blue solid line unit-cell) formed on top of the Au(111) surface (grey, dotted) surrounded by hexagonal superstructure spots. Due to the larger ionic radius of the RE atom compared to that of the Au atom, the registry with the Au(111) plane underneath is lost, and a coincidence moiré lattice appears.[1] The periodicity of this moiré reconstruction is visible in the LEED pattern through the characteristic satellite spots around the main $(\sqrt{3} \times \sqrt{3})R30°$ diffraction spots. The atomic misfit is also obvious when comparing the clean and the compound-covered surface patterns, as shown in Fig. 1(a), where the new atomic spacing of the surface is compared to that of Au(111).

In STM micrographs two main features are observed, namely the atomically resolved lattice of the surface and the large scale moiré modulation rotated by 30° with respect to the atomic unit cell. Atomically resolved images reveal hexagonal close-packed structures with a = 5.4 Å periodic spacing between neighboring protrusions, which clearly indicates that

‡This is especially needed to avoid Gd bulk impurities that reemerge at the Au surface during annealing cycles.

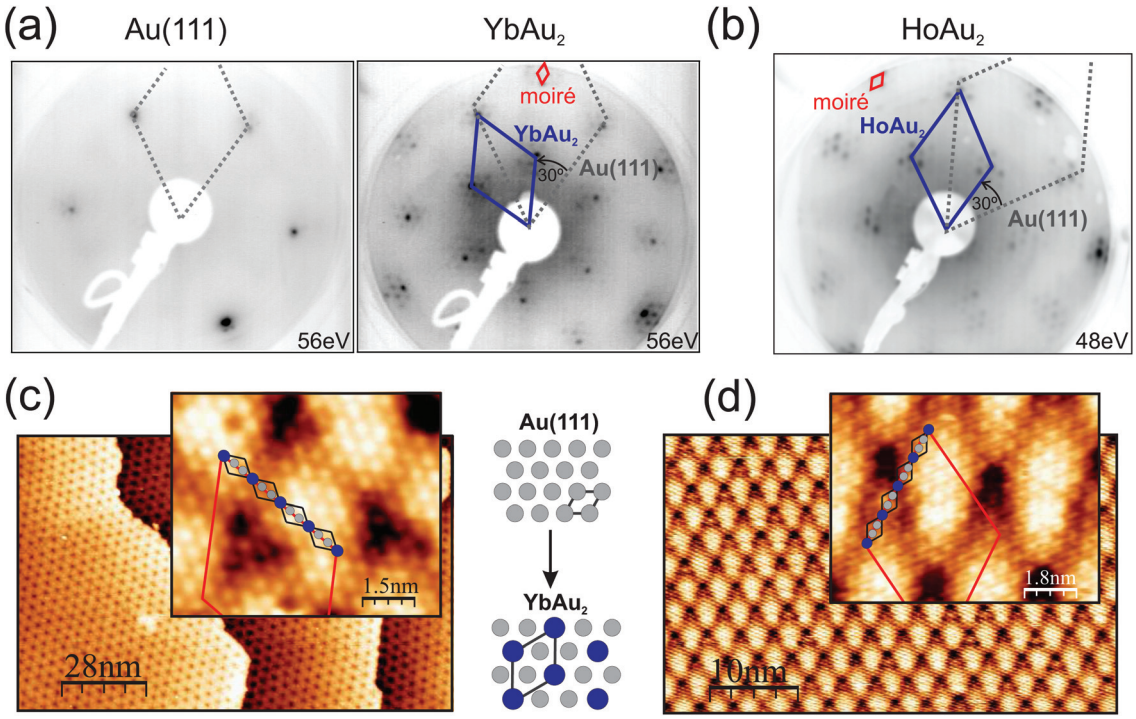

Fig. 1 Structural analysis of $YbAu_2$ and $HoAu_2$ by low-energy electron diffraction (a and b) and scanning tunneling microscopy (c and d), respectively. In the LEED image of the clean Au(111) the small satellite spots originate from the herringbone reconstruction. Rare-earth deposition results in the periodic substitution of Au in the topmost atomic layer (see the sketch), defining a $(\sqrt{3} \times \sqrt{3})R30°$ unit cell. The grey and blue rhombuses in the LEED patterns mark the Au(111) and the RE-Au_2 reciprocal space lattices, respectively. The insets of the STM images reveal atomic resolution, with RE atoms appearing as bright protrusions (marked with black rhombuses). A ~(13 × 13) moiré superstructure is observed in both LEED and STM. Its moiré lattice is indicated with small and large red rhombuses in the respective panels. The moiré reflects the overlayer/substrate lattice mismatch, induced by the larger RE ionic diameter compared to that of Au. The larger interatomic distance in the $REAu_2$ monolayer is mirrored in a reduced spacing between the main LEED spots as compared to the separation in Au(111). The kinetic energy of the LEED experiments is indicated. STM images were acquired under a bias voltage of −1.2 V and a tunneling current of 1.4 nA.

only the RE sublattice is being probed by the STM tip under the present conditions.[33] The same apparent atomic lattice is observed in the previously studied $GdAu_2$, $CeAu_2$, $LaAu_2$, $TbAu_2$, $HoAu_2$ and $ErAu_2$ monolayers.[1,2,6,33] The moiré periodicities of $YbAu_2$ and $HoAu_2$ have been determined by averaging over large scale STM images such as those of Fig. 1(c) and (d), rendering (36.5 ± 1.0) Å and (37.6 ± 1.0) Å, respectively. The latter value coincides well with a recent study of $HoAu_2$.[6] Taking into account the interatomic distance in the Au(111) surface (a_{Au} = 2.89 Å) one obtains a (12.6 × 12.6) coincidence lattice for $YbAu_2$ and a slightly larger (13.0 × 13.0) lattice for $HoAu_2$, the latter being equal to that found in $GdAu_2$.[1] The lattice constant a of the RE-Au_2 surface lattice can be extracted from the RE-Au_2/Au(111) $(n-1)/n$ coincidence through $(n-1) \times a = n \times \sqrt{3}a_{Au}$ leading to a = 5.4 Å in $HoAu_2$, $YbAu_2$, and $GdAu_2$ monolayers.[1] Differences in the moiré periodicity, though, reflect subtle variations in the interatomic distance a of the compound, which cannot be accounted for within the STM accuracy. In this respect, the shorter beating period for the $YbAu_2$ monolayer reveals a 0.3% larger in-plane interatomic spacing. This indeed is the simple expectation for the larger ionic radius of the divalent Yb. However, the effect is very small and may also arise due to other important factors, such as the out-of-plane relaxation of the RE sublattice,[34] similar to that observed in Rashba type systems.[35]

3.2. Electronic properties

3.2.1. Core level analysis and rare earth valency. The valence state of the RE atom for each $REAu_2$ compound is assessed through the analysis of its respective 5p and 4f shallow core levels. Fig. 2 shows the photoemission spectra around the 4f and 5p core level regions for $GdAu_2$, $HoAu_2$, and $YbAu_2$ monolayers. Electron energies refer to the Fermi level. To properly separate the 4f core-level emission from that of other electronic states in the valence band of the compound and the Au substrate (mainly 5d), spectra were acquired at photon energies corresponding to on- and off-resonance[40] (blue and red lines, respectively). For the RE 5p levels no resonant photoemission is needed, as it falls far away from the Fermi level where no Au substrate related emission occurs. As usually found in RE metals and compounds, 4f and 5p peaks are not simple spin–orbit split emissions but reveal photoemission multiplets. Ionization of the partially filled 4f orbitals leads to a variety of final states in the $4f^{n-1}$ configuration, and hence to the multiplet structures.[41] The multiplets calculated in the intermediate coupling regime[36] are shown for Gd,

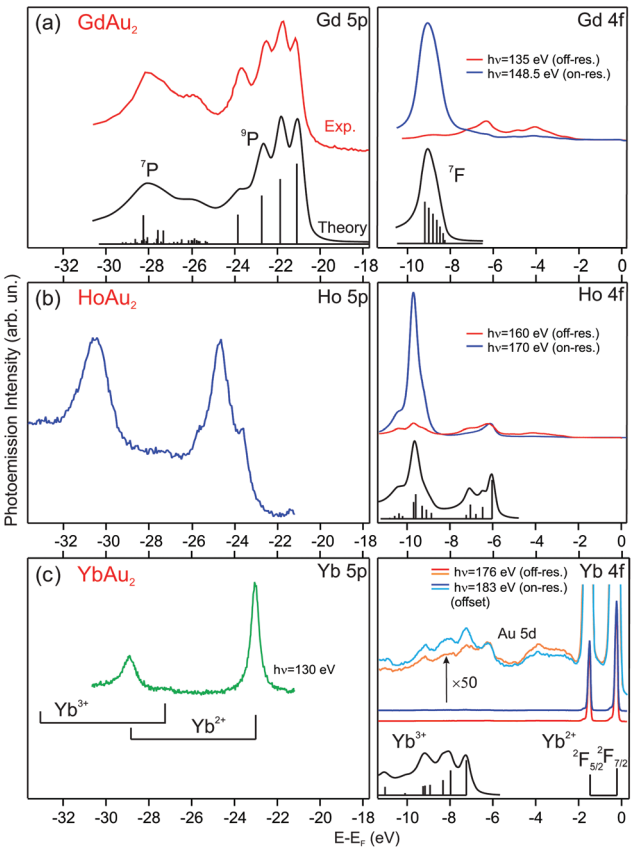

Fig. 2 Photoemission spectra taken at T = 17 K of 5p and 4f rare-earth core levels for (a) $GdAu_2$, (b) $HoAu_2$, and (c) $YbAu_2$ monolayers grown on Au(111). The valence state of the rare-earth atom can be determined by comparing with theoretically calculated multiplets, shown under the corresponding spectra (multiplet data reproduced from ref. 20 and 36–39).

Ho and Yb in Fig. 2 (solid black curves). Binding energies of the calculated spectra have been shifted to the experimental values. Generally speaking, the appearance of 4f emission close to E_F indicates a divalent configuration in RE atoms, while multiplets at binding energies higher than 5 eV correspond to the RE trivalent state. In the case of the RE 5p peaks, these emissions also exhibit multiplets and result from final state photoemission effects.[42] After photo-excitation of a 5p electron, the hole left behind interacts with the electrons in unfilled subshells resulting in different final states that lead to the observed 5p multiplet.

In the $GdAu_2$ monolayer, Gd 4f and 5p levels are similar to the calculated and experimentally observed multiplet structures of trivalent Gd metal.[38,39] The effect of alloying with Au in the surface compound can be directly assessed by comparison to the surface core level lines in the corresponding RE metal crystals, where RE atoms at the surface have the same atomic coordination (ninefold) but a Au environment within the surface plane. The trivalent Gd 4f and 5p lines of $GdAu_2$ are shifted to higher binding energies by 0.6 eV and 0.7 eV, respectively, with respect to the corresponding surface core levels in metal Gd.[43] For $HoAu_2$ the situation is very similar. The Ho 4f multiplet reveals a trivalent character and it is shifted to a higher binding energy by 0.4 eV with respect to the surface component in metallic Ho.[44]

The valence state for Yb in $YbAu_2$ is deduced by directly comparing the experimental spectrum with the theoretical di- and trivalent configurations of Yb, shown in the lower part of Fig. 2(c). In the surface compound, there is a dominant divalent Yb 4f emission near E_F, although a zoom in the spectrum reveals the presence of trivalent Yb emission at a higher binding energy. An accurate determination of the trivalent contribution is difficult, since the trivalent multiplet overlaps with the Au 5d band. The Yb 5p core level, however, is better suited for a quantitative analysis. On- and off-resonant photoemission reveals a small, but well visible, trivalent $5p_{3/2}$ emission at 27.24 eV. This binding energy discards emission from bulk Yb impurities,[20] and rather indicates a mixed valence scenario, with a dominant divalent state and a minor trivalent contribution (for a detailed discussion see the ESI†). X-ray photoemission is a fast femtosecond-range transition process, particularly when compared to the valence fluctuation time of rare-earth ions in mixed-valence systems.[45] Such fluctuation time can be estimated from the valence band dispersion (see the ESI†). Therefore, the relative peak area of the two 5p doublets in Fig. 2(c) directly reflects an intermediate valence value $\bar{\nu}$ = 2.059 of the Yb valence in $YbAu_2$.

The Yb 5p and 4f core levels in $YbAu_2$ are shifted to lower binding energies by 1.15 eV and 1.55 eV, respectively, compared with the corresponding surface core levels in metallic Yb.[37] The positive shift of the core level in $YbAu_2$ with respect to the corresponding divalent Yb surface contrasts with the negative shift in trivalent Gd and Ho emissions as shown above. The valency-dependent sign of the shift from the pure metal to compound in RE core levels was already observed for a variety of divalent and trivalent bulk RE-metal systems.[37] The sign of the shift can be explained by the larger structural stability of the trivalent RE ion, *versus* divalent or tetravalent states, when forming bulk compounds.[37,46] In this way, the trivalent-to-tetravalent core-level photoemission process of Gd and Ho leads to a negative peak shift, while the divalent-to-trivalent excitation in Yb results in a positive shift.

3.2.2. Band structure. The electronic band structure of the $GdAu_2$, $HoAu_2$ and $YbAu_2$ monolayers on Au(111) is measured by ARPES, and is displayed in Fig. 3 and 4. ARPES bands of $GdAu_2$ were already investigated and discussed in ref. 2, 3, 33 and 47. Fig. 3 displays the electronic band structure of $HoAu_2$ as measured by ARPES in the synchrotron with different photon energies at a sample temperature of 17 K, together with the bands measured with $h\nu$ = 21 eV (HeIα) at 120 K. We focus in the energy range between the Fermi energy and E_F − 2 eV in order to avoid the high intensity of the substrate Au 5d-bands. The lack of dispersive changes across the different panels in Fig. 3(a) caused by different photon energies proves the two-dimensional character of most characteristic $HoAu_2$ bands, namely those labeled as A, B, C and C′. The B band appears away from the Fermi level with a strong Au bulk-like character. The A band is found at the border but still inside the projected

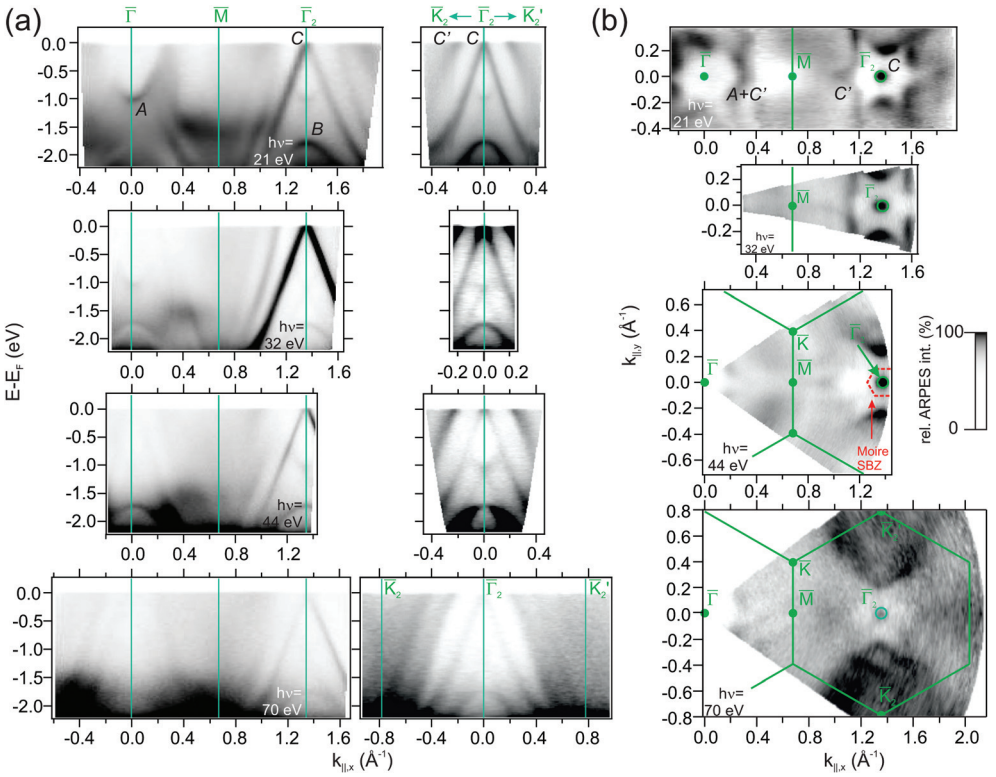

Fig. 3 Angle-resolved photoemission (ARPES) maps for 1 ML $HoAu_2$/Au(111): (a) band dispersion along the $\bar{\Gamma}\bar{M}\bar{\Gamma}_2$ and the $\bar{K}_2\bar{\Gamma}_2\bar{K}_2$ direction of the surface Brillouin zone taken for different photon energies. (b) Fermi energy band crossing mappings for the same indicated energies. The $(13/12\cdot\sqrt{3} \times 13/12\cdot\sqrt{3})$R30° surface Brillouin zones [with respect to Au(111)] appear indicated with green lines. Albeit the sample temperature (17 K) is below the Curie temperature T_C = 22 K of $HoAu_2$ (see below), the band splitting due to magnetic exchange appears to be too small to be detected.

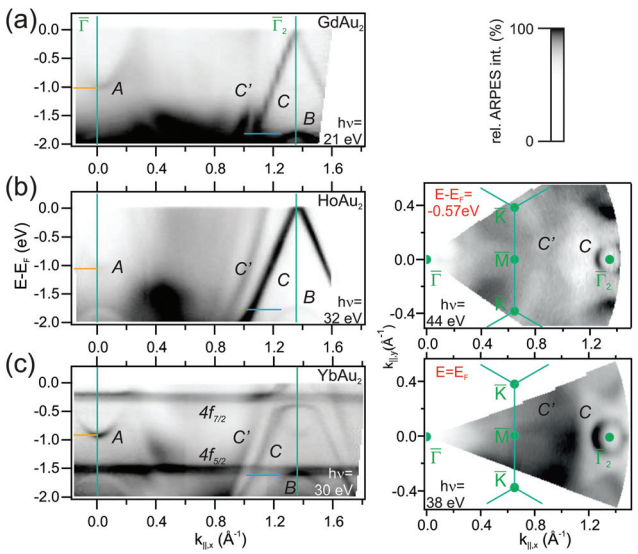

Fig. 4 (a) Band dispersion along the $\bar{\Gamma}\bar{M}\bar{\Gamma}_2$ reciprocal space direction for (a) $GdAu_2$, (b) $HoAu_2$, and (c) $YbAu_2$ monolayers, as determined from ARPES experiments performed at the indicated photon energies in each case. In the right panels, constant energy intensity maps for $HoAu_2$ at $E - E_F$ = 0.57 eV and $YbAu_2$ at E_F are displayed featuring similar features at the $\bar{\Gamma}_2$-point. $GdAu_2$ bands were measured at T = 120 K, while $HoAu_2$ and $YbAu_2$ experiments were carried out at T = 17 K.

substrate band gap, and therefore has a surface character, with a mixed Au and RE wave-function nature.[3] Its dispersion and position are very similar to the Shockley surface state of noble metal surfaces[48] when shifted to higher binding energy upon deposition of, *e.g.*, alkali metals.[49,50] Finally, the hole-like, linearly-dispersing C band crosses E_F around $\bar{\Gamma}$, where it strongly resonates at the $HoAu_2$ surface. The $GdAu_2$ valence band exhibits the same features,[33] including the intense linearly-dispersing C band. Other RE-Au_2 surface compounds such as $LaAu_2$ and $CeAu_2$ possess the same C band with a conic shape centered at $\bar{\Gamma}$ and apex at E_F.[2] In reality, as indicated in Fig. 4(a) and (b), $REAu_2$ monolayers featuring trivalent RE atoms share an almost identical band structure, including the hole-like B and electron-like A bands, the latter found at −1.0 eV at the center of the Brillouin zone in all cases.[2] Even the Fermi surface mappings shown in Fig. 3(b) are similar, showing a bright spot due to the C band apex, and a star-shaped feature around the $\bar{\Gamma}$ points, originating from the A and C′ bands. In a recent study,[51] this star-shaped feature was attributed to umklapp bands from the $(\sqrt{3} \times \sqrt{3})$ R30° surface superstructure replica of the strongly dispersive noble metal s,p band. However, the latter is a bulk band that disperses perpendicular to the surface in k_z direction. This would give rise to different Fermi energy features at different photon energies,[52–54] but this is not observed here (see Fig. 3 and the ESI†). Our theoretical analysis (see below)

reveals that C′ has an intense Au s,p-band nature. We argue that the strong band hybridization with RE d-bands changes not only the band character of C′ but also alters the k_z dispersion into a two-dimensional band. Additionally, one can also observe the umklapp bands due to the moiré superstructure. The moiré umklapp bands cause the "X"-like band crossing feature at $E - E_F = -1.2$ eV located at the second $\bar{\Gamma}$-points of the surface Brillouin zones. A detailed discussion can be found in the ESI.†

For divalent Yb in $YbAu_2$, the narrow 4f bands shows up right below E_F ($4f_{7/2}$) and at $E - E_F = -1.5$ eV ($4f_{5/2}$), giving rise to relatively flat bands. Especially the $4f_{7/2}$ level strongly hybridizes with the C band, leading to a large disruption of its linear dispersion around the Fermi energy. This additionally affects the Fermi surface around $\bar{\Gamma}$ in Fig. 4, which evolves from an intense spot in trivalent $HoAu_2$ [see Fig. 3(b)] to a ring-shaped structure in divalent $YbAu_2$. Also the Au bulk-resonating s,p band (C′) reveals band hybridization and an upward shift. The latter can be nicely observed by comparing the band crossings at the Fermi energy in $YbAu_2$ and the constant energy surface at $E - E_F = -0.57$ eV of $HoAu_2$ featuring similar structures. Valency-dependent differences in the electronic states of $REAu_2$ monolayer systems, from trivalent Gd, La, Ce, and Ho, to divalent Yb, are also found in A and B bands, which exhibit upward shifts of 0.11 and 0.15 eV, respectively, from trivalent compounds to divalent Yb.

The hybridization of 4f levels with the s–p–d valence-band many fold has often been observed in three-dimensional bulk Ce, Eu and Yb compounds.[55,56] Orbital mixing with 4f levels at the valence band gives rise to an intermediate fluctuating valence in RE materials,[45] which in turn is essential to trigger competing magnetic phases around quantum-critical points.[57] In Fig. 5 we examine in detail the 4f level hybridization for the two-dimensional $YbAu_2$ compound, comparing ARPES and first principles calculations. In panel (a) we show the $YbAu_2$ ARPES band dispersion along the $\bar{\Gamma}\bar{M}\bar{\Gamma}_2$ and $\bar{K}_2\bar{\Gamma}_2\bar{K}_{2'}$ symmetry lines, on top of the corresponding calculations for a $YbAu_2$/3ML-Au(111) slab [(b) panel]. To better determine the surface or bulk nature of the different bands, in panel (c) we show their evolution from the free-standing $YbAu_2$ monolayer, to the $YbAu_2$/1ML-Au(111) and $YbAu_2$/3ML-Au(111) stacks. In the free standing case, one observes the conic C band dispersing from about 0.7 eV above E_F at $\bar{\Gamma}$ down to −2 eV at $\bar{M}$ and $\bar{K}$. This C band is intercepted by the flat Yb 4f levels. As the number of gold layers in the stack increases, the f levels slightly shift towards E_F while the C band shifts downward, spin–orbit splitting sets in, and the more bulk-like C′ band builds up. In fact, the C′ band is significantly contributed by Gd-d electrons, sharing with C a partial $s,p_{x,y}$–$d_{x,y}$ mixed orbital nature, but the occupied part of C lies inside the Au bulk projected band gap and resonates stronger at the $YbAu_2$ surface.§ Additionally, C and C′ mix with the spin–orbit split 4f levels at about −0.25 eV, leading to a clear opening of hybridization gaps (see the discussion on the d and f composition of these hybrid bands in the ESI†). The relative contribution of the 4f levels to the different bands is graphically indicated with a color scale in Fig. 5. The upward shift of the 4f spectral weight leads to a small but relevant 4f spread above E_F, thereby explaining the occurrence of mixed valence. It is interesting to note that the DFT approach is enough to properly describe experimental binding energies and anticrossing features,[58] even though, at the present theory level, one cannot account for simultaneous divalent and trivalent 4f multiplets in the valence band (for DFT band structures including correlation, which causes renormalization and an increase in bandwidth,[59] see the ESI†).

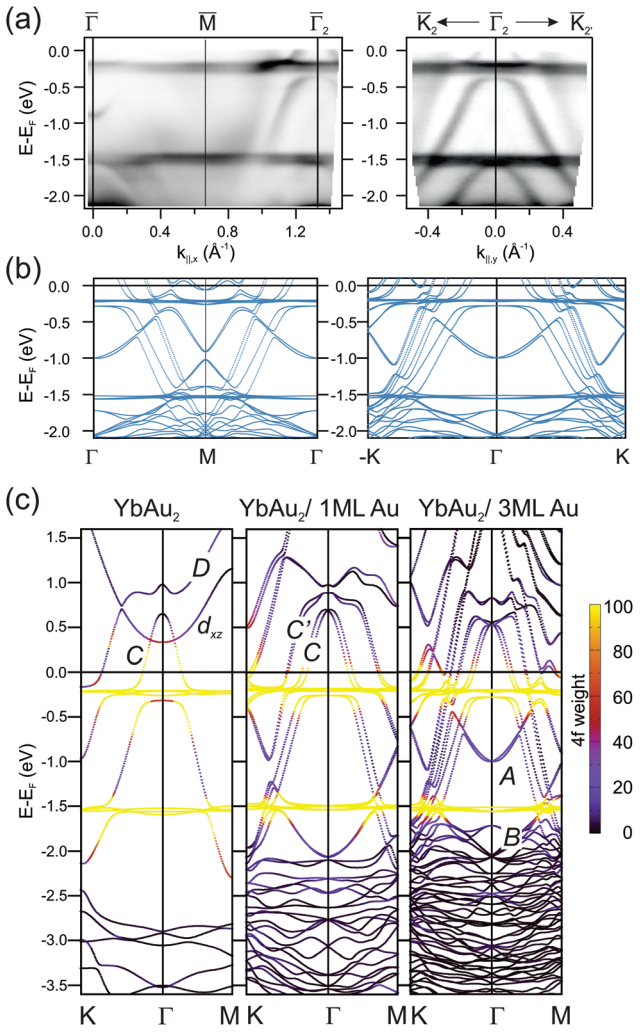

Fig. 5 (a) ARPES band dispersions for the $YbAu_2$ monolayer compound measured along the $\bar{\Gamma}\bar{M}\bar{\Gamma}_2$ and $\bar{K}_2\bar{\Gamma}_2\bar{K}_{2'}$ symmetry directions of the surface Brillouin zone ($h\nu$ = 38 eV, T = 17 K). (b) Corresponding DFT band structure calculated for a $YbAu_2$/3ML-Au(111) slab. Spin–orbit interactions with spins aligned perpendicular to the surface are included. (c) DFT band structure for a free-standing $YbAu_2$ monolayer (left), a $YbAu_2$/1ML-Au(111) bilayer (center), and the $YbAu_2$/3ML-Au(111) stack (right). The 4f composition of each $E(k)$ point is indicated by the violet-to-yellow color scale. Bands are named following ref. 2 and 33.

§ In ref. 3 C′ labels the spin minority branch of C in ferromagnetic $GdAg_2$ and $GdAu_2$. Here, C′ refers to a different bulk resonating band.

On the other hand, bands A and B, which only emerge with the thickest Au slab, also interact with the 4f levels, although such interaction is not clearly resolved in the ARPES experiment. Finally, we must also note the presence of the D and the upward dispersing band of d_{xz} character. The last one crosses C without hybridizing (orthogonal to C) in the free standing case. The D band has mainly $d_{x^2-y^2}$ character and hybridizes with the states at the apex of the C band of d_{xy} character forming a gapped region close to the Γ point at around E_F + 0.7 eV (details on the orbital character can be found in the ESI†). In terms of orbital character, the aforementioned band crossing features are ubiquitous in RE-Au_2 layers and give rise to the magnetic and topological properties of these systems. However, the dispersion details and binding energies differ for different compounds and some of such characteristic features are likely to disappear upon hybridization with substrate bands. For example, in the $GdAg_2$/Ag(111) system the spin–split pair of D bands straddle the Fermi energy, contributing to the ferromagnetic order at high temperature (T_C = 85 K),[3] and resulting in several degeneracies that have been reported to be Weyl nodal lines.[60] We recall that Weyl points are massless Dirac fermions that appear in pairs of opposite parity, protected by the lattice translational symmetry. Additional mirror symmetry can stabilize Weyl points in a two-dimensional system,[61] as it has been reported for $GdAg_2$, where band degeneracies of this type appear close to the Fermi level not as discrete points, but forming a line, so-called Weyl nodal line.[60] In $GdAg_2$ and $ErCu_2$ the upward-dispersing spin-majority d_{xz} band and the downward-dispersing spin-minority C mutually cross near the Fermi level, defining topologically protected Weyl nodal lines.[5,60] Furthermore, the gap formed at the crossing of C and D bands with opposite spin polarization in $GdAg_2$ is stable even against a reorientation of the magnetization from in-plane to out-of-plane.[60] Note, however, that the equivalent feature in the $YbAu_2$ layer is strongly distorted by the much larger spin–orbit interaction strength. As mentioned above, the nodal line associated with this C–D crossing in the free-standing $YbAu_2$ case would be a ring near the Γ-point well above the Fermi level E_F + 0.7 eV due to the divalent Yb, with a large energy gap of 0.2 eV [see Fig. 5(c)]. ARPES is not suited to probe empty electronic states and we are therefore unable to confirm such theoretical prediction. For the $GdAu_2$ case DFT calculations revealed that the nodal line is at 0.3 eV below the Fermi level.[3] The C–D band crossing has a band gap of nearly 0.1 eV with in-plane magnetization, but a marginal one with out-of-plane magnetization, in agreement with the prediction based on the orbital symmetries of these two bands.[62] Because of the Fermi level proximity and the small size of the band gap, this feature is not distinguishable by ARPES.

3.3. Magnetic configuration

Rare-earth metals and alloys exhibit diverse magnetic properties across the RE series, explained by the strong effect of the variable 4f shell filling. When combining RE with noble metals long range magnetic ordering was observed for $GdAu_2$,[8,64] $GdAg_2$,[3] and $DyAg_2$.[51] For completely divalent Yb compounds with a filled 4f shell no magnetic moments from that 4f shell can arise, *e.g.*, the pure hcp Yb metal (divalent) is diamagnetic at least down to 1 K.[65] We therefore do not expect magnetic ordering in the accessible temperature range (T > 4 K) for $YbAu_2$, although here Yb is in a mixed-valent state.

In the following, we will concentrate on the magnetic properties and magnetic anisotropy of $HoAu_2$ measured by X-ray absorption (XAS) and magnetic circular dichroism (XMCD) and compare the results to the magnetic properties observed in $GdAu_2$. To shortly summarize, $GdAu_2$ is a two-dimensional, soft ferromagnetic system with a Curie temperature T_C = 19 K, and an in-plane easy magnetization axis.[3,8] DFT calculations[3,64] and low temperature STM measurements at applied fields[64] reveal that the long-range order arises from the polarization of both Gd and Au derived valence electrons by the localized Gd 4f moments *via* a RKKY-type interaction. The coercive field H_c in $GdAu_2$ is small ranging from 2 mT (ref. 3) to 17.5 mT (ref. 64) depending on the number of defects like dislocation lines at the surface.

For the $HoAu_2$ monolayer case XAS and XMCD spectra are shown in Fig. 6. The XAS line shape in Fig. 6(a) confirms a trivalent Ho $4f^{10}$ configuration[66] already observed by photoemission. There are remarkable differences between normal and grazing incidence geometries. The dichroism is larger at normal incidence indicating an out-of-plane easy axis, which is corroborated in the XMCD magnetization loops displayed in Fig. 6(b). In the XAS spectra, both, M_4 and M_5 absorption edges (3d → 4f) display the same sign of the dichroism in the two different geometries with the magnetic field and X-ray

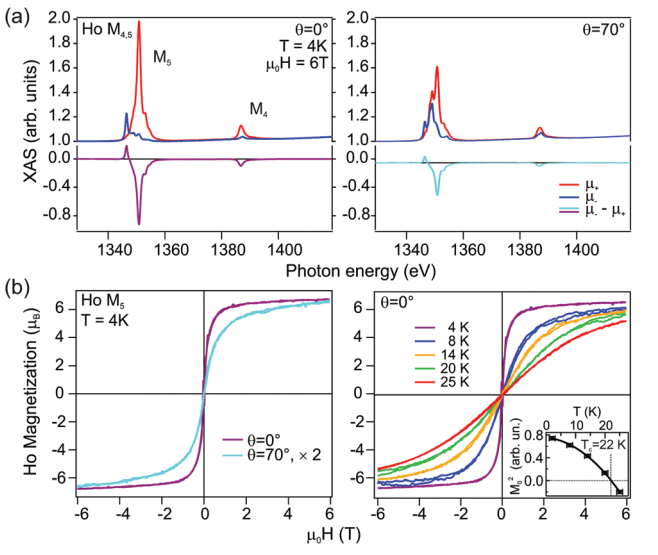

Fig. 6 (a) X-ray Magnetic Circular Dichroism (XMCD) in absorption spectra measured at the Ho $M_{4,5}$ edge in normal (θ = 0°, left) and grazing beam incidence (θ = 70°, right). (b) Magnetization curves acquired at the M_5 edge at different incidence geometries (left), and at normal incidence with variable temperature (right). The dependence on the incidence angle reveals ferromagnetic behavior with out-of-plane easy axis. The Arrott plot analysis[3,63] of the magnetization curves at different temperatures renders the Curie temperature T_C = 22 K (inset).

Table 1 Orbital L_z, spin S_z and total J_z angular moments of $HoAu_2$ compared to Ho single atoms on different metal surfaces as determined from sum rule analysis. Data correspond to coplanar field and light incidence normal to the surface θ = 0° (NI), grazing incidence θ = 70° for $HoAu_2$, and θ = 60° for literature values[14,15] (GI)

System	$\langle L_z\rangle^{NI}$	$\langle S_z\rangle^{NI}$	$\langle J_z\rangle^{NI}$	$\langle L_z\rangle^{GI}$	$\langle S_z\rangle^{GI}$	$\langle J_z\rangle^{GI}$
$HoAu_2$	(5.26 ± 0.15)	(1.52 ± 0.12)	(6.78 ± 0.19)	(2.62 ± 0.10)	(0.76 ± 0.08)	(3.38 ± 0.13)
Ho/Cu(111)[14,15]	(5.3 ± 0.2)	(1.7 ± 0.1)	(6.9 ± 0.2)	(3.8 ± 0.1)	(1.1 ± 0.1)	(4.9 ± 0.1)
Ho/Ag(111)[15]	(5.2 ± 0.1)	(1.2 ± 0.2)	(6.5 ± 0.2)	(4.8 ± 0.1)	(1.2 ± 0.1)	(6.0 ± 0.1)
Ho/Pt(111)[14,15]	(4.3 ± 0.1)	(1.3 ± 0.1)	(5.5 ± 0.1)	(3.8 ± 0.1)	(1.3 ± 0.1)	(5.1 ± 0.1)

incidence perpendicular (θ = 0°) and nearly parallel (θ = 70°) to the surface. Such a situation is expected for late lanthanides ($4f^n$, $n > 7$). These late lanthanides are characterized by a large magnetic moment arising from the parallel alignment of the orbital L and spin S components leading to the total angular momentum $J = L + S$. The expectation values of the orbital and spin magnetic moments components on the magnetization axis z, $\langle L_z\rangle$ and $\langle S_z\rangle$, respectively, can be obtained from sum rules analysis of the integrated XAS and XMCD spectra (see ESI†) and are given in Table 1. For the sake of comparison we also include literature values of single Ho atoms on top of fcc (111) surfaces of noble metals Cu, Ag, and Pt.[14,15] The paramagnetic-to-ferromagnetic transition in $HoAu_2$ is tracked from the series of out-of-plane magnetization loops at different temperatures shown in the right panel of Fig. 6(b). An Arrott plot analysis of these magnetization curves[3,63] leads to a Curie temperature T_C = 22 K (see details in the ESI†).

For the ideal Ho^{3+} ion with a $4f^{10}$ configuration, Hund's rule predicts orbital and spin moments of L = 6 and S = 2, respectively, resulting in a total angular moment J = 8 and oblate form of the 4f charge distribution when the J_z value is maximal.[67,68] We observe a normal incidence (NI) ground state value along the field direction z of $\langle J_z\rangle^{NI}$ = 6.78 for the $HoAu_2$ surface compound (see Table 1), which is very similar to the values measured in Ho single adatoms on Cu(111)[14] and Ag(111) surfaces[15] but different from the Ho/Pt(111) case.[14] For Ho/Cu(111) and Ho/Ag(111) the Ho 4f electron charge density distribution is barely influenced by hybridization with substrate bands formed by delocalized s electrons. Thus, neither the form of the 4f electron charge distribution density, nor the lowest J ground state, is affected. In the case of the $HoAu_2$ monolayer, trivalent Ho atoms embedded in the Au surface have a similar environment as Ho adatoms on Ag (111) and Cu(111) surfaces. As can be observed in Table 1, there is, however, a difference in the grazing incidence (in-plane) value of the surface compound, whose magnetic moments are much lower. This difference is related to the measurement geometry that in the actual $HoAu_2$ case was for more grazing incidence (θ = 70°) than in the adatom cases (θ = 60°).

The out-of-plane easy-axis anisotropy of $HoAu_2$ monolayer contrasts with the in-plane one of $GdAu_2$.[8] The main contribution to the magnetic anisotropy in both surface compounds has a different nature that is directly related to the RE 4f occupation and its angular momentum. Trivalent Gd^{3+} ions have a half-filled $4f^7$ shell with L = 0 and therefore have a completely isotropic (spherical) 4f electron charge distribution. In this case the main contribution to the magnetocrystalline anisotropy of $GdAu_2$ arises from the hybrid Au–Gd bands and results in a magnetocrystalline anisotropy energy of about 2.7 meV.[8] Certainly, in-plane shape anisotropy is also present, but its contribution is minor with an approximate value of 0.05 meV (see the ESI†). In the case of $HoAu_2$, however, the anisotropy originates at the 4f electrons, as suggested by the large L. The observed out-of plane anisotropy may be explained in simple terms by the spatial distribution of the 4f electron cloud. As already mentioned, for a free trivalent Ho^{3+} ion with a $4f^{10}$ configuration the 4f electron density has an oblate shape with the highest J_z level. Additionally, the electrostatic interaction with the Au substrate electron density would favour out-of-plane anisotropy, while the equatorially distributed charge density within the $HoAu_2$ layer would favour in-plane anisotropy.[14] All together, the substrate, $HoAu_2$ layer charges and the oblate form of the 4f cloud at high J_z favour out-of-plane anisotropy[68–70] as observed by the sum rule result $J_z^{NI} \gg J_z^{GI}$ (see Table 1).

4. Conclusions

$HoAu_2$ and $YbAu_2$ monolayer compounds have been synthesized by vapor deposition onto Au(111), and analyzed with surface science techniques and DFT calculations. The resulting structural, electronic and magnetic properties have been compared with those of the $GdAu_2$/Au(111). In all cases we find a $(\sqrt{3} \times \sqrt{3})$ R30° RE substitution in the topmost Au(111) crystal layer, which triggers analogous nanoscale moiré superstructures, due to mismatch with the underlying substrate. Through X-ray photoemission of valence and core levels we determine a trivalent state for Gd and Ho, and a mixed-valence situation of Yb in $YbAu_2$. Electronic band structures are nearly equivalent for the three surface compounds, with the exception of their characteristic conic C band near E_F, which strongly hybridizes with the 4f level in $YbAu_2$. DFT indicates that such f–d hybridization results in a small depletion of the Yb 4f shell in $YbAu_2$, which appears to explain its mixed valence character. Moreover, XMCD experiments reveal a ferromagnetic ordering in $HoAu_2$ with an out-of-plane anisotropy below T_C = 22 K. The origin of the out-of-plane anisotropy in $HoAu_2$ is mainly magnetocrystalline due to the strong spin–orbit coupling interaction of the 4f electrons in Ho and their electrostatic interaction with the surrounding charge.

Author contributions

L. F. and F. S. conceived and designed the work. L. F., R. C.-B., K. A., E. T., M. C., M. O., P. M., P. M. S., A. K. K., M. J. and F. S. carried out photoemission data collection while the data were analyzed and interpreted by P. M. S., M. O., C. L., E. O. and F. S. X-ray absorption and XMCD data collection were undertaken by L. F., R. C.-B., M. I., P. G., M. A. V., A. M., and F. S. The DFT calculations were performed by M. B.-R. The analysis of these data was carried out by F. S. and the results were interpreted by L. F., M. B.-R., A. M., E. O. and F. S. The article was drafted by L. F., M. B.-R., E. O. and F. S. All authors contributed in the critical revision of the article and its final approval.

Conflicts of interest

There are no conflicts to declare.

Acknowledgements

This work was supported in part by the Spanish MINECO (MAT-2017-88374-P, MAT2016-78293-C6, FIS2016-75862-P, PGC2018-098613-B-C21, SEV-2017-0706 and SEV-2016-0686), the Spanish Research Agency (PID2019-107338RB-C65), Basque Government Project IT-1255-19, and University of the Basque Country (UPV/EHU) grant GIU18/138 and the European Regional Development Fund (ERDF) under the program Interreg V-A España-Francia-Andorra (Contract No. EFA 194/16 TNSI). The experiments at Elettra were supported by the EU Calipso project and computational resources were provided by the DIPC computing center. L. F. acknowledges financial support from the European Union's Horizon 2020 research and innovation programme under the Marie Skłodowska-Curie grant agreement MagicFACE No 797109. A. K. K., M. J., P. M. S. and P. M. acknowledge the project EUROFEL-ROADMAP ESFRI. We furthermore want to thank Prof. T. Greber from the University of Zürich to enable us to use the ARPES spectrometer for the constant energy and Fermi surface measurements.

References

1 M. Corso, L. Fernández, F. Schiller and J. E. Ortega, *ACS Nano*, 2010, **4**, 1603–1611.
2 M. Ormaza, L. Fernández, S. Lafuente, M. Corso, F. Schiller, B. Xu, M. Diakhate, M. J. Verstraete and J. E. Ortega, *Phys. Rev. B: Condens. Matter*, 2013, **88**, 125405.
3 M. Ormaza, L. Fernández, M. Ilyn, A. Magaña, B. Xu, M. J. Verstraete, M. Gastaldo, M. A. Valbuena, P. Gargiani, A. Mugarza, A. Ayuela, L. Vitali, M. Blanco-Rey, F. Schiller and J. E. Ortega, *Nano Lett.*, 2016, **16**, 4230–4235.
4 A. Correa, B. Xu, M. J. Verstraete and L. Vitali, *Nanoscale*, 2016, **8**, 19148–19153.
5 C. Xu, K. Bao, Y. Que, Y. Zhuang, X. Shao, K. Wang, J. Zhu and X. Xiao, *Phys. Chem. Chem. Phys.*, 2020, **22**, 1693–1700.
6 Y. Que, Y. Zhuang, Z. Liu, C. Xu, B. Liu, K. Wang, S. Du and X. Xiao, *J. Phys. Chem. Lett.*, 2020, **11**, 4107–4112.
7 M. Urdampilleta, S. Klyatskaya, J.-P. Cleuziou, M. Ruben and W. Wernsdorfer, *Nat. Mater.*, 2011, **10**, 502.
8 L. Fernández, M. Blanco-Rey, M. Ilyn, L. Vitali, A. Magaña, A. Correa, P. Ohresser, J. E. Ortega, A. Ayuela and F. Schiller, *Nano Lett.*, 2014, **14**, 2977–2981.
9 L. Fernández, M. Corso, F. Schiller, M. Ilyn, M. Holder and J. E. Ortega, *Appl. Phys. Lett.*, 2010, **96**, 013107.
10 A. Cavallin, L. Fernández, M. Ilyn, A. Magaña, M. Ormaza, M. Matena, L. Vitali, J. E. Ortega, C. Grazioli, P. Ohresser, S. Rusponi, H. Brune and F. Schiller, *Phys. Rev. B: Condens. Matter*, 2014, **90**, 235419.
11 L. Fernández, M. Ilyn, A. Magaña, L. Vitali, J. E. Ortega and F. Schiller, *Adv. Sci.*, 2016, **3**, 1600187.
12 Q. Si and F. Steglich, *Science*, 2010, **329**, 1161–1166.
13 T. Miyamachi, T. Schuh, T. Märkl, C. Bresch, T. Balashov, A. Stöhr, C. Karlewski, S. André, M. Marthaler, M. Hoffmann, M. Geilhufe, S. Ostanin, W. Hergert, I. Mertig, G. Schön, A. Ernst and W. Wulfhekel, *Nature*, 2013, **503**, 1476–4687.
14 F. Donati, A. Singha, S. Stepanow, C. Wäckerlin, J. Dreiser, P. Gambardella, S. Rusponi and H. Brune, *Phys. Rev. Lett.*, 2014, **113**, 237201.
15 A. Singha, R. Baltic, F. Donati, C. Wäckerlin, J. Dreiser, L. Persichetti, S. Stepanow, P. Gambardella, S. Rusponi and H. Brune, *Phys. Rev. B*, 2017, **96**, 224418.
16 F. Donati, S. Rusponi, S. Stepanow, L. Persichetti, A. Singha, D. M. Juraschek, C. Wäckerlin, R. Baltic, M. Pivetta, K. Diller, C. Nistor, J. Dreiser, K. Kummer, E. Velez-Fort, N. A. Spaldin, H. Brune and P. Gambardella, *Phys. Rev. Lett.*, 2020, **124**, 077204.
17 W.-D. Schneider, C. Laubschat and B. Reihl, *Phys. Rev. B: Condens. Matter*, 1983, **27**, 6538–6541.
18 G. Kaindl, G. Kalkowski, W. D. Brewer, B. Perscheid and F. Holtzberg, *J. Appl. Phys.*, 1984, **55**, 1910–1915.
19 R. Pöttgen, D. Johrendt and D. Kußmann, *Structure-property relations of ternary equiatomic YbTX intermetallics*, Elsevier, 2001, ch. 207, vol. 32, pp. 453–513.
20 G. K. Wertheim, J. H. Wernick and G. Crecelius, *Phys. Rev. B: Condens. Matter*, 1978, **18**, 875–879.
21 S. Chatterjee, J. P. Ruf, H. I. Wei, K. D. Finkelstein, D. G. Schlom and K. M. Shen, *Nat. Commun.*, 2017, **8**, 2041.
22 D. V. Vyalikh, S. Danzenbächer, Y. Kucherenko, C. Krellner, C. Geibel, C. Laubschat, M. Shi, L. Patthey, R. Follath and S. L. Molodtsov, *Phys. Rev. Lett.*, 2009, **103**, 137601.
23 T. Greber, O. Raetzo, T. J. Kreutz, P. Schwaller, W. Deichmann, E. Wetli and J. Osterwalder, *Rev. Sci. Instrum.*, 1997, **68**, 4549–4554.
24 J. P. Perdew, K. Burke and M. Ernzerhof, *Phys. Rev. Lett.*, 1996, **77**, 3865–3868.
25 FLEUR: http://www.flapw.de.
26 H. Krakauer, M. Posternak and A. J. Freeman, *Phys. Rev. B: Condens. Matter*, 1979, **19**, 1706–1719.
27 E. Wimmer, H. Krakauer, M. Weinert and A. J. Freeman, *Phys. Rev. B: Condens. Matter*, 1981, **24**, 864.

28 C. Li, A. J. Freeman, H. J. F. Jansen and C. L. Fu, *Phys. Rev. B: Condens. Matter*, 1990, **42**, 5433.
29 H. J. Monkhorst and J. D. Pack, *Phys. Rev. B: Condens. Matter*, 1976, **13**, 5188.
30 V. I. Anisimov, F. Aryasetiawan and A. I. Liechtenstein, *J. Phys.: Condens. Matter*, 1997, **9**, 767.
31 A. B. Shick, A. I. Liechtenstein and W. E. Pickett, *Phys. Rev. B: Condens. Matter*, 1999, **60**, 10763.
32 V. I. Anisimov, I. V. Solovyev, M. A. Korotin, M. T. Czyzyk and G. A. Sawatzky, *Phys. Rev. B: Condens. Matter*, 1993, **48**, 16929.
33 M. Corso, M. J. Verstraete, F. Schiller, M. Ormaza, L. Fernández, T. Greber, M. Torrent, A. Rubio and J. E. Ortega, *Phys. Rev. Lett.*, 2010, **105**, 016101.
34 A. Correa, M. F. Camellone, A. Barragan, A. Kumar, C. Cepek, M. Pedio, S. Fabris and L. Vitali, *Nanoscale*, 2017, **9**, 17342–17348.
35 I. Gierz, B. Stadtmüller, J. Vuorinen, M. Lindroos, F. Meier, J. H. Dil, K. Kern and C. R. Ast, *Phys. Rev. B: Condens. Matter*, 2010, **81**, 245430.
36 F. Gerken, *J. Phys. F: Met. Phys.*, 1983, **13**, 703–713.
37 C. Laubschat, G. Kaindl, W.-D. Schneider, B. Reihl and N. Mårtensson, *Phys. Rev. B: Condens. Matter*, 1986, **33**, 6675–6683.
38 W. J. Lademan, A. K. See, L. E. Klebanoff and G. van der Laan, *Phys. Rev. B: Condens. Matter*, 1996, **54**, 17191–17198.
39 G. van der Laan, E. Arenholz, E. Navas, Z. Hu, E. Mentz, A. Bauer and G. Kaindl, *Phys. Rev. B: Condens. Matter*, 1997, **56**, 3244–3250.
40 S. R. Mishra, T. R. Cummins, G. D. Waddill, W. J. Gammon, G. van der Laan, K. W. Goodman and J. G. Tobin, *Phys. Rev. Lett.*, 1998, **81**, 1306–1309.
41 P. A. Cox, J. K. Lang and Y. Baer, *J. Phys. F: Met. Phys.*, 1981, **11**, 113–119.
42 B. T. Thole, X. D. Wang, B. N. Harmon, D. Li and P. A. Dowben, *Phys. Rev. B: Condens. Matter*, 1993, **47**, 9098–9101.
43 G. A. Mulhollan, K. Garrison and J. L. Erskine, *Phys. Rev. Lett.*, 1992, **69**, 3240–3243.
44 G. Kaindl, A. Höhr, E. Weschke, S. Vandré, C. Schüßler-Langeheine and C. Laubschat, *Phys. Rev. B: Condens. Matter*, 1995, **51**, 7920–7923.
45 J. M. Lawrence, P. S. Riseborough and R. D. Parks, *Rep. Prog. Phys.*, 1981, **44**, 1–84.
46 B. Johansson, *Phys. Rev. B: Condens. Matter*, 1979, **19**, 6615.
47 M. Abadía, M. Ilyn, I. Piquero-Zulaica, P. Gargiani, C. Rogero, J. E. Ortega and J. Brede, *ACS Nano*, 2017, **11**, 12392–12401.
48 F. Reinert, G. Nicolay, S. Schmidt, D. Ehm and S. Hüfner, *Phys. Rev. B: Condens. Matter*, 2001, **63**, 115415.
49 S. A. Lindgren and L. Walldén, *Solid State Commun.*, 1978, **28**, 283–286.
50 F. Schiller, M. Corso, M. Urdanpilleta, T. Ohta, A. Bostwick, J. L. McChesney, E. Rotenberg and J. E. Ortega, *Phys. Rev. B: Condens. Matter*, 2008, **77**, 153410.
51 J. Knippertz, P. M. Buhl, S. Mousavion, B. Dupé, E. S. Walther, K. Medjanik, D. Vasilyev, S. Babenkov, M. Ellguth, M. Maniraj, J. Sinova, G. Schönhense, H.-J. Elmers, M. Aeschlimann and B. Stadtmüller, *Exchange Splitting of a Hybrid Surface State and Ferromagnetic Order in a 2D Surface Alloy*, 2019, arXiv:1906.03780.
52 P. Aebi, J. Osterwalder, R. Fasel, D. Naumović and L. Schlapbach, *Surf. Sci.*, 1994, **307–309**, 917–921.
53 A. Stampfl, J. Foo, R. Leckey, J. Riley, R. Denecke and L. Ley, *Surf. Sci.*, 1995, **331–333**, 1272–1276.
54 J. Osterwalder, *Surf. Rev. Lett.*, 1997, **04**, 391–408.
55 S. Danzenbächer, D. V. Vyalikh, Y. Kucherenko, A. Kade, C. Laubschat, N. Caroca-Canales, C. Krellner, C. Geibel, A. V. Fedorov, D. S. Dessau, R. Follath, W. Eberhardt and S. L. Molodtsov, *Phys. Rev. Lett.*, 2009, **102**, 026403.
56 S. Danzenbächer, D. V. Vyalikh, K. Kummer, C. Krellner, M. Holder, M. Höppner, Y. Kucherenko, C. Geibel, M. Shi, L. Patthey, S. L. Molodtsov and C. Laubschat, *Phys. Rev. Lett.*, 2011, **107**, 267601.
57 Z. Hossain, C. Geibel, N. Senthilkumaran, M. Deppe, M. Baenitz, F. Schiller and S. L. Molodtsov, *Phys. Rev. B: Condens. Matter*, 2004, **69**, 014422.
58 M. Matsunami, T. Hajiri, H. Miyazaki, M. Kosaka and S. Kimura, *Phys. Rev. B: Condens. Matter*, 2013, **87**, 165141.
59 H. Schweitzer and G. Czycholl, *J. Magn. Magn. Mater.*, 1988, **76–77**, 77–79.
60 B. Feng, R.-W. Zhang, Y. Feng, B. Fu, S. Wu, K. Miyamoto, S. He, L. Chen, K. Wu, K. Shimada, T. Okuda and Y. Yao, *Phys. Rev. Lett.*, 2019, **123**, 116401.
61 S. Nie, H. Weng and F. B. Prinz, *Phys. Rev. B*, 2019, **99**, 035125.
62 E. Abate and M. Asdente, *Phys. Rev.*, 1965, **140**, A1303–A1308.
63 A. Arrott, *Phys. Rev.*, 1957, **108**, 1394–1396.
64 M. Bazarnik, M. Abadia, J. Brede, M. Hermanowicz, E. Sierda, M. Elsebach, T. Hänke and R. Wiesendanger, *Phys. Rev. B*, 2019, **99**, 174419.
65 E. Bucher, P. H. Schmidt, A. Jayaraman, K. Andres, J. P. Maita, K. Nassau and P. D. Dernier, *Phys. Rev. B: Condens. Matter*, 1970, **2**, 3911–3917.
66 B. T. Thole, G. van der Laan, J. C. Fuggle, G. A. Sawatzky, R. C. Karnatak and J.-M. Esteva, *Phys. Rev. B: Condens. Matter*, 1985, **32**, 5107–5118.
67 J. Tang and P. Zhang, *Lanthanide Single Molecule Magnets*, Springer, Berlin, Heidelberg, 2015.
68 J. D. Rinehart and J. R. Long, *Chem. Sci.*, 2011, **2**, 2078–2085.
69 D. Givord, *Europhys. News*, 1987, **18**, 93–96.
70 R. Skomski and D. Sellmyer, *J. Rare Earths*, 2009, **27**, 675–679.